Optimal Observations for Variational Data Assimilation

ARMIN KÖHL AND DETLEF STAMMER

Scripps Institution of Oceanography, La Jolla, California

(Manuscript received 25 November 2002, in final form 23 June 2003)

ABSTRACT

An important part of ocean state estimation is the design of an observing system that allows for the efficient study of climate related questions in the ocean. A solution to the design problem is presented here in terms of optimal observations that emerge as singular vectors of the modified data resolution matrix. The actual computation is feasible only for scalar quantities and in the limit of large observational errors. Identical twin experiments performed in the framework of a 1° North Atlantic primitive equation model demonstrate that such optimal observations, when applied to determining the heat transport across the Greenland–Scotland ridge, perform significantly better than traditional section data. On seasonal to interannual time scales, optimal observations are located primarily along the continental shelf and information about heat transport, wind stress, and stratification is being communicated through boundary waves and advective processes. On time scales of about 1 month, sea surface height observations appear to be more efficient in reconstructing the cross-ridge heat transport than hydrographic observations. Optimal observations also provide a tool for understanding changes of ocean state associated with anomalies of integral quantities such as meridional heat transport.

1. Introduction

Through spaceborne measurements and through global programs such as the World Ocean Circulation Experiment (WOCE) and Tropical Ocean and Global Atmosphere (TOGA), we now have a data-rich environment that is unprecedented in the history of ocean research and includes altimetry (Fu and Cazenave 2001) and a global profiling float program (ARGO; see Roemmich and Owens 2000) as the backbone of a climate ocean observing system. However, to answer many scientific questions, our database will remain insufficient (in time and space) and many quantitative climate studies must rely on a model–data synthesis (data assimilation) as a basis to compute observable and unobservable climate aspects. Required for climate studies are assimilation methods that are rigorous in a mathematical sense and take into account errors in data and the model alike without violating trustworthy dynamical principles. Among these approaches is that of the Pontryagin principle, usually known as variational data assimilation, or the adjoint method. Only then can we compute important characteristics such as the variability of oceanic transport properties, of transport convergences, and other aspects of the large-scale circulation, such as changes of the meridional overturning circulation and its impact on climate.

Corresponding author address: Dr. Armin Köhl, Scripps Institution of Oceanography, University of California, San Diego, 9500 Gilman Drive, La Jolla, CA 92093-0230.
E-mail: akoehl@ucsd.edu

The traditional use of the adjoint procedure in oceanography is that of data synthesis. However, an important question with respect to a global synthesis is that of the design of an optimal observing system, that is, the determination of the combination of various different observations and their geographical distribution that constrain ocean circulation models in the most effective way. Assessing an observing system in the context of the adjoint method is equivalent to assessing the impact of specific data types and their location on the convergence rate of the optimization and to evaluating the sensitivity of the converged solution to additional data. Although any such observing system design will critically depend on the specific scientific question that leads to the formulation of the cost function, many features of the ocean's flow field are large scale, influencing climate through integral quantities. It is therefore hoped that any single basis for a climate observing system will impact many different climate aspects through the combination (in space and time) of ocean observations with model dynamics.

To date only a few studies exist that have approached the design of an observing system in a systematic way. Among those are Barth and Wunsch (1990), who employed a simulated annealing method for the configuration of an acoustic tomography array, and Schröter and Wunsch (1986), who used inequality constraints as a cost function for which the sensitivity of the cost function to data is represented by adjoint sensitivities. This approach describes the framework within which the following recent works of Marotzke et al. (1999)

and Lee et al. (2002) can be interpreted. Both publications suggest that the adjoint sensitivities of the heat transport to model state variables (e.g., temperature, salinity or velocity) may be used to identify regions in which hydrographic measurements or the knowledge of surface forcing are key for determining changes in the heat transport itself. Adjoint sensitivities determine the relative importance of specific control variables (e.g., initial conditions or forcing) on a specified scalar quantity, such as meridional heat transport. For instance, anomalous heat transport could be caused by either kinematic or dynamic anomalies of the ocean state (Marotzke et al. 1999) or can originate from anomalous forcing conditions (Lee et al. 2002).

The value of adjoint sensitivities comes from the ability to predict the future evolution of the ocean state or, more specifically, a certain aspect of the circulation, from observations collected in the past. Generally it is of interest to infer integrative quantities such as transports and it is often much easier to deduce anomalies of these quantities from their effects on the ocean state. This classical hindcast situation is of general importance for oceanographic applications and design methods need to be developed in this framework. Adjoint sensitivities are helpful for observing system designs only as far as the controls can be identified directly with data [e.g., Marotzke et al. (1999) identifies sensitivities to the temperature initial condition with preferred locations for temperature observations]. Moreover, those sensitivities do not take into account uncertainties in the observations or the model. For this reason a fundamental difference exists in how data are used in state estimations and how the link to sensitivities is established.

In contrast to ocean applications, the recent interest in observing system design in atmospheric science is mainly driven by the goal of improving short-term weather forecasts, and in general, existing methods attempting to reduce the variance of the error. The concept of adaptive observations was first introduced by Snyder (1996). Various techniques exist including singular vectors (Palmer 1998), adjoint sensitivities (Baker and Daley 2000), Kalman filter methods, and others (Berliner et al. 1999).

The purpose of this paper is to discuss an ocean observing system design that determines the observations that are most influential to the estimation of specific circulation aspects using the variational estimation approach. Although the method presented is derived in general and therefore universally applicable, we focus in a first application on the determination of observations that in a model simulation allow us to monitor in a most effective way the heat transport across the Greenland–Scotland ridge.

Exchange processes across the Greenland–Scotland ridge (Hansen and Østerhus 2000) are important for the determination of hydrographic conditions south and north of the sills and more generally the maintenance of the meridional overturning circulation (MOC). The Denmark Strait Overflow Water (DSOW) and Iceland–Scotland Overflow Water (ISOW) contribute to the formation of North Atlantic Deep Water (NADW) that moves equatorward at depth and affects the thermohaline structure of the global ocean. Although the role of the Greenland–Iceland–Scotland (GIN) Seas in NADW formation and in determining our present and future climate seems to be widely accepted (Dickson and Brown 1994), a detailed understanding of 1) the degree of transport variations and 2) adjustment processes of the flow over the Greenland–Scotland ridge (GSR) to changing forcing conditions over the GIN Seas has not yet been established. However, several indications exist for longterm changes of the overflow characteristics and of the hydrography in the adjacent regions (Dickson et al. 2002; Bacon 1998; Hansen et al. 2001). Biastoch et al. (2003, hereinafter BKS) discuss the sensitivity of that transport to changes in wind forcing over the subpolar gyre and to cross-ridge density gradients. We here determine in a model simulation the observational data base required to monitor changes of transports across Greenland–Scotland ridge.

The structure of the paper is as follows: section 2 explains the concept of optimal observations; the model framework in which the concept will be applied is summarized in section 3. In section 4 we discuss the interannual to decadal variability of the cross-ridge transports as they follow from a 50-yr-long model simulation. In section 5 a set of observations is then constructed that are required to determine those changes in the best possible way. In section 6 the efficiency of optimal data distribution is finally tested in an assimilation experiment, and the relative importance of different observational variables is discussed in section 7.

2. The concept of optimal observations

To introduce the notation we will start with a brief summary of variational data assimilation and then provide a compact description of optimal observations, that is, observations that constrain a model in an optimal way. For a detailed account on inverse modeling in oceanography see Wunsch (1996), Fukumori (2001), and Bennett (2002).

Define an ocean general circulation model (OGCM) as

$$\frac{\partial x}{\partial t} = f(x, \alpha), \tag{1}$$

where x is the model state, and α is a vector of control parameters. Observations are related to the model state through the observational matrix $\mathbf{E}$ as

$$y = \mathbf{E}x + n, \tag{2}$$

where n is the noise in the observations. In essence, the estimation procedure finds control parameters (α) that are required to bring the model trajectory into consis-

tency with noisy observations and with an imperfect model. Those control parameters usually include uncertain quantities such as the model initial conditions, surface and lateral boundary conditions, or model mixing parameters.

To proceed, we linearize the model (1) around an a priori set of control parameters, α^o, which might be a result of an already performed data assimilation or parameters from an existing simulation. Since we are working in a linearized framework, it is crucial that the parameter and the corresponding trajectory are already skillful. The dependency of changes of the trajectory δx to changes $\delta\alpha$ may then be represented as

$$\delta x = \mathbf{F}\delta\alpha. \tag{3}$$

Kleeman and Moore (1997), in their introduction to the derivation of stochastic optimals, show how one can go from a classical form (1) to this notation. Here $\delta\alpha = \alpha - \alpha^o$, $\delta x = x - x^o$, and x^o is the model trajectory for the set of control parameters α^o. Changes in $\delta\alpha$, δx, and δy are assumed here to be small. Similar to a linear propagator, $\mathbf{F}$ is not just a local (in time and space) operator, but involves a convolution of $\delta\alpha$ in space and time. For almost any application of ocean state estimation which involves a full nonlinear OGCM, this relation is too complex to be provided in a complete form. However, an approximation of $\mathbf{F}$ was explicitly calculated by Stammer and Wunsch (1996).

The parameter improvement $\delta\alpha$ might in principle be written in terms of the observations y or, equivalently, the initial model data difference

$$\delta y = y - \mathbf{E}x^o. \tag{4}$$

The relation

$$\delta\alpha = \mathbf{B}\delta y, \tag{5}$$

is the solution of the optimization problem which minimizes the norm of δy upon adding further constraints and which is given in a more explicit form below. By combining (5) with (3), a linear mapping from the observational space onto the space of model trajectories,

$$\delta x = \mathbf{FB}\delta y = \mathbf{A}\delta y, \tag{6}$$

is obtained. The modified data resolution matrix $\mathbf{A}$ ($\mathbf{EA}$ would be the true data resolution matrix) maps observations, expressed as model–data differences, onto trajectory improvements of the model. It projects the information that is contained in the observations onto the state or changes of the state to the extent to which they are included in the model dynamics. Menke (1989) already proposed the resolution matrix as a useful tool for experimental design.

Optimal observation locations are then described by the singular vectors of the matrix $\mathbf{W}^{-1/2}\,\mathbf{A}$, where $\mathbf{W}$ is the inverse of the error covariance of the data and where the square root is defined as the matrix, which has the same eigenvectors as $\mathbf{W}$ and has the square root of the eigenvalues of $\mathbf{W}$ as eigenvalues. The term ''optimal'' in this respect means that these observations would impose maximal changes on the trajectory δx when assimilated in a variational assimilation system. The matrix $\mathbf{W}^{-1/2}$ takes measurement errors for different data types into account.

Calculating singular vectors of $\mathbf{A} = \mathbf{FB}$ in the generality of the last paragraph is in general too expensive in the context of a full nonlinear OGCM. We now restrict applications to cases where the model state is projected onto a single scalar quantity, $h(x)$, such as meridional heat transport in the ocean. Then the dependency of h on the data y can be described by the gradient $\partial h/\partial y$ itself, which corresponds to the resolution matrix $\mathbf{A}$ in (6) since only one aspect of the trajectory x is evaluated. Because the gradient is a vector, the calculation of singular vectors are not necessary. It can be written as the product of two terms,

$$\frac{\partial h}{\partial y} = \frac{\partial h}{\partial \alpha}\frac{\partial \alpha}{\partial y}; \tag{7}$$

both will be treated separately in the following.

In the same way as the adjoint operator $\mathbf{F}^{\mathrm{T}}$ is used in the adjoint model to calculate gradients of the cost function with respect to the parameter α, the first term

$$\left(\frac{\partial h}{\partial \alpha}\right)^{\mathrm{T}} = \left(\frac{\partial h}{\partial x}\frac{\partial x}{\partial \alpha}\right)^{\mathrm{T}} = \mathbf{F}^{\mathrm{T}}\left(\frac{\partial h}{\partial x}\right)^{\mathrm{T}} \tag{8}$$

can be calculated by replacing the cost function with h. Note that $\partial h/\partial x$ is in general a simple relation which does not involve the integration of any dynamical model.

In order to approximate the second part, a more explicit expression for the inverse relation (5) is required. With $\mathbf{W}$ and $\mathbf{V}$ describing the weight (i.e., inverse of the error covariance of the data and the parameter), the cost function can be written as

$$J = \frac{1}{2}(\delta\alpha)^{\mathrm{T}}\mathbf{V}\delta\alpha + \frac{1}{2}(y - \mathbf{E}x)^{\mathrm{T}}\mathbf{W}(y - \mathbf{E}x) \tag{9}$$

and the Lagrangian follows as

$$L = J + \lambda(\delta x - \mathbf{F}\delta\alpha), \tag{10}$$

where we made use of the linearized version (3) of the model.

A general solution that minimizes (9) can be written as

$$\delta\alpha = \mathbf{V}^{-1}\mathbf{F}^{\mathrm{T}}\mathbf{E}^{\mathrm{T}}(\mathbf{W}^{-1} + \mathbf{EFV}^{-1}\mathbf{F}^{\mathrm{T}}\mathbf{E}^{\mathrm{T}})^{-1}\delta y. \tag{11}$$

(see Menke 1989). In this notation, no explicit model error term is provided and model adjustments are only obtained through the adjustment of the controls. The actual measurement error part in $\mathbf{W}^{-1}$ is, in general, far smaller than acceptable model adjustments—$\mathbf{EFV}^{-1}\mathbf{F}^{\mathrm{T}}\mathbf{E}^{\mathrm{T}}$ could be neglected in comparison to $\mathbf{W}^{-1}$ (note that $\mathbf{W}$ is the inverse observational error covariance). For most applications, however, $\mathbf{W}^{-1}$ is mainly determined by representation and model errors which

cannot be represented by the adjustment of the controls. The latter can be, especially for coarse-resolution models, in the same order or even larger than the anticipated model adjustments.

To proceed, we postulate that $\mathbf{EFV}^{-1}\mathbf{F}^{\mathrm{T}}\mathbf{E}^{\mathrm{T}}$ can even be neglected in comparison to $\mathbf{W}^{-1}$. The relation (11) is thus evaluated for the limit of large observational errors (this includes the model error), which is in accord with our initial assumption that the new state is close to the first guess x^{o}. While this assumption is made here to allow a considerable simplification, it is justified below by determining and testing the optimal observations in identical twin experiments. With the latter approximation, (11) reduces to

$$\delta\alpha = \mathbf{V}^{-1}\mathbf{F}^{\mathrm{T}}\mathbf{E}^{\mathrm{T}}\mathbf{W}\delta y. \tag{12}$$

We note that (12) does not involve a full inversion of the model, but only the calculation of weighted forcing anomalies from one backward calculation of the adjoint model $\mathbf{F}^{\mathrm{T}}$ that is driven by the weighted model–data differences $\mathbf{W}\delta y$.

Combining (12) with (8) yields the final result

$$\left(\frac{\partial h}{\partial y}\right)^{\mathrm{T}} = \mathbf{WEFV}^{-1}\mathbf{F}^{\mathrm{T}}\left(\frac{\partial h}{\partial x}\right)^{\mathrm{T}}. \tag{13}$$

This relation involves the adjoint $\mathbf{F}^{\mathrm{T}}$ and a linearized version $\mathbf{F}$ of the forward model. The construction of the linearized model $\mathbf{F}$ is a similar effort as the construction of an adjoint.

However, starting from a full nonlinear model we seek to avoid this step by a finite difference approach. The procedure starts with a forward run and the application of one optimization step employing the gradient $\mathbf{F}^{\mathrm{T}}\partial h/\partial x$ calculated by the adjoint to reduce h. The optimization step requires a normalization that involves the weight $\mathbf{V}$ of the control parameter. The step size of the parameter innovation $\delta\alpha$ should be small enough to keep the trajectory of the second forward run with the new parameter set in the vicinity of the trajectory of the initial forward run. This is easy to achieve since the optimization algorithm estimates a step size. The difference of the resulting trajectories then approximates the trajectory of the linearized model $\mathbf{F}$. After projecting onto the observations (matrix $\mathbf{E}$) and scaling with the weight $\mathbf{W}^{1/2}$, this difference is proportional to $\mathbf{W}^{-1/2}\partial h/\partial y$. In summary, the calculation of optimal observations involves in principle a single iteration of the variational assimilation procedure completed by a projection and weighting step. It is a necessary condition that the cost function h is actually reduced during this step, which is, in general, guaranteed for small enough a step size. Preferred data locations are identified by the extreme values of the gradient $\mathbf{W}^{1/2}\partial h/\partial y$ and observations at those locations will reduce the difference of the quantity of interest h maximally when used in a variational data assimilation system. In addition to the choice of h and y, optimal observations also depend on the configuration of the data assimilation system. This primarily includes the model configuration (e.g., resolution, domain, and parameterizations), the choice of the weights, the set of control variables, and the integration period. The relative error of data types (e.g., temperature vs salinity) or of certain parameters (e.g., wind stress vs heat flux) is of profound importance as it directly affects the importance of certain data types.

The use of optimal observations does not necessarily imply that the quantity of interest is estimated with the greatest precision, which would certainly be the ultimate goal for selecting observations. Optimal observations defined by the maximum gradient criterion are, by definition, preferable in cases where measurement errors (including representation and model error) are large and where only sparse data sampling, either in time or space, is available. We finally note that the validity of this method is limited by the linearization approach, which implies an upper limit for the integration time when applied with chaotic models (Li 1991; Stensrud and Bao 1992)—for example, eddy-resolving models.

3. Model framework

The design of optimal observations and their evaluation of the performance in reconstructing a scalar quantity requires all components necessary for ocean state estimate—that is, the forward model, its adjoint, the model–data interface, and an optimization procedure. The numerical model was developed at the Massachusetts Institute of Technology (MIT) and is described by Marshall et al. (1997). It is based on the primitive equations in a z-coordinate formulation and is operated here in a hydrostatic mode with an implicit free surface and partial bottom cells implemented [see Adcroft et al. (1997) for details]. The model code is designed to allow the construction of the adjoint using the automatic differentiation tool TAMC (Giering and Kaminski 1998). Marotzke et al. (1999) describe in detail the adjoint model generation. Stammer et al. (2002, 2003; 2004, manuscript submitted to *J. Geophys. Res.*) describe a first global state estimation attempt with this model. The quasi-Newton optimization algorithm used to calculate the control vector change for each iteration is described by Gilbert and Lemaréchal (1989).

The model used in this study covers the North Atlantic Ocean from 20°S to 76°N and has a realistic bottom topography based on the ETOPO5 (1988) dataset. The spatial resolution is 1° in longitude and 1° $\cos\phi$ in latitude. The thickness of the 37 vertical levels increases smoothly from 11 m at the surface to 250 m below 1000 m. Closed northern and southern boundaries as well as the Strait of Gibraltar have a 5° restoring zone attached in which potential temperature and salinity are relaxed toward monthly mean values of Levitus and Boyer (1994) and Levitus et al. (1994). Horizontal and vertical viscosity is parameterized by Laplacian mixing with values of 10^4 and 10^{-3} m^2 s^{-1}, respectively. The horizontal

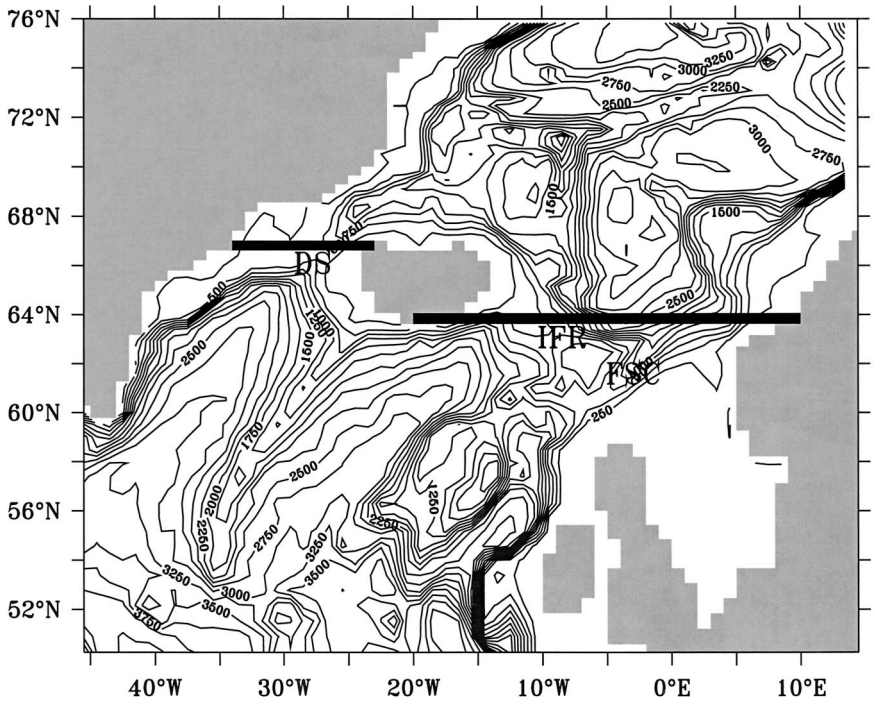

FIG. 1. Model bathymetry for the region around Iceland (contour interval = 250 m) with the main passages: Denmark Strait (DS), Iceland–Faore Ridge (IFR), and Faroe–Shetland Channel (FSC). The section across which the heat and volume transports are calculated is marked.

diffusivity is set to $10^3\ \mathrm{m^2\ s^{-1}}$; in the vertical a Laplacian diffusivity of $10^{-3}\ \mathrm{m^2\ s^{-1}}$ was prescribed in combination with a convective adjustment scheme.

The model was forced with once per day surface heat and virtual salt fluxes as provided by the National Centers for Environmental Prediction (NCEP)–National Center for Atmospheric Research (NCAR) reanalysis project (Kalnay et al. 1996). Daily shortwave heat flux is prescribed separately from turbulent heat flux contributions; its vertical profile of absorption is modeled by the analytical formula of Paulson and Simpson (1977) for prescribed time-dependent ocean water types after Jerlov (1968). An additional relaxation term is introduced to relax surface temperature and surface salinity toward the monthly mean values of the climatology with a 30-day time scale. Wind stress fields are twice per day.

Equation (9) requires prior information about data and model errors. The weights **W** and **V** are approximated by the error profiles for temperature and salinity taken from Levitus and Boyer (1994) and Levitus et al. (1994). They smoothly decrease from about 1°C and 0.27 psu at the surface to 0.1°C and 0.02 psu in depth. Error values for the surface forcing fields were assumed to be constant in space and time and were given values of 100 W $\mathrm{m^{-2}}$, 1×10^{-7} m $\mathrm{s^{-1}}$ and 0.05 N $\mathrm{m^{-2}}$ for the heat flux, salinity flux, and the wind stress components, respectively.

The model was started in January 1948 from rest with initial conditions for temperature and salinity taken from Levitus and Boyer (1994) and Levitus et al. (1994) and integrated for 50 yr, driven by NCEP–NCAR reanalysis fluxes at the surface. Years with specifically high or low transport values were selected from this reference run to serve as data in identical twin experiments. The set of control parameters in all our experiments comprises initial conditions for temperature and salinity and monthly mean corrections for the forcing fields. All subsequent experiments as well as the calculation of optimal observations were carried out over the period of the year 1990.

4. Greenland–Scotland ridge transports simulations

In the next sections we will analyze observations that are required to optimally determine variations of GSR transport variations. But before we do so, we will first provide a description of transport variations as they occur in the 50-yr-long model simulation and discuss underlying physical mechanisms. The model bathymetry for the area around Iceland depicted in Fig. 1 shows the three main passages of the GSR, which are the Denmark Strait (DS) east of Iceland, the Iceland–Faore Ridge (IFR), and the Faroe–Shetland Channel (FSC) on the west side. The sections across which the heat transport is calculated are indicated by the bold lines in the figure.

The flow through DS and the subsequent down slope flow along the topography depend on processes that are not sufficiently resolved in most models and are essen-

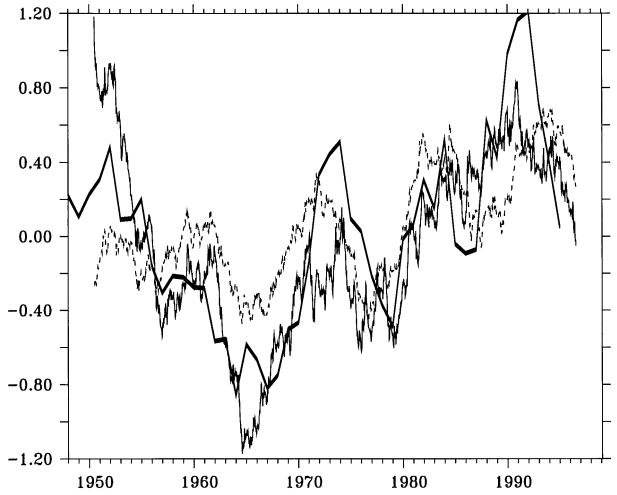

FIG. 2. Anomalies with respect to the 50-yr mean of GSR heat transport (solid; 10 TW), southward volume transport through Denmark Strait channel (dashed; Sv $\equiv 10^6$ m^3 s^{-1}), and 0.5 $\times$ NAO index (bold). All three curves were smoothed with a 5-yr running mean to filter high-frequency fluctuations. The remaining signal accounts for about 10% of the total variability. The mean heat transport is 0.10 PW and the mean southward volume transport is 6.5 Sv.

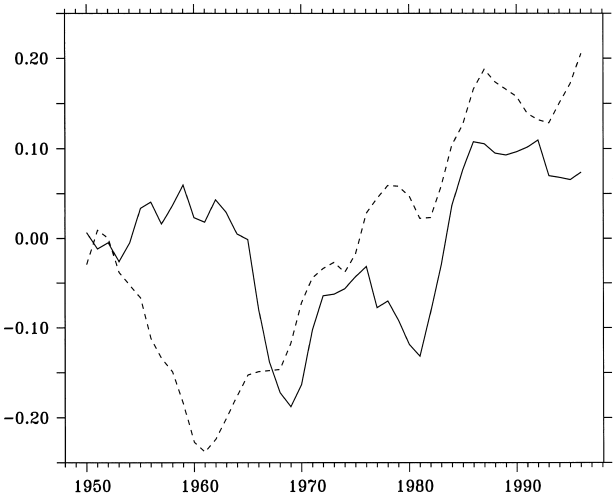

FIG. 3. Anomalies of potential temperature θ (°C) averaged vertically over the water column and over the model domain for 60°–66.75°N, 50°–10°W (dashed) and 66.75°–70°N, 50°–10°W (solid). Both curves were smoothed with a 5-yr running-mean filter to remove high-frequency fluctuations.

tially absent in our 1° version of the MIT model. Specifically, the *z*-coordinate formulation of the MIT model represents the downward flow by consecutive convective adjustment steps which entails substantial mixing. Water masses are therefore not conserved downstream of the sill and a realistic hydraulic control overflow mechanism is absent. However, the simulated transport values may still be in a realistic range. For the present model an estimated time-mean barotropic transport of cold and fresh water through DS strait at 65.4°N of 4.4 Sv (1 Sv $\equiv 10^6$ m^3 s^{-1}) agrees well with results from Käse and Oschlies (2000) of 4 Sv. At 65.5°N it consists of 1.9 Sv inflow (Irminger Current) and 6.3 Sv outflow (East Greenland Current and overflow) of which 2.1 Sv is below 2.2°C. The net outflow through the DS is balanced by inflow of the warm and saline North Atlantic Current, which separates east of Iceland into the Faroe Current (4.8 Sv) and the Shetland Current (2.2 Sv). The eastern overflow follows two paths across the IFR and through the FSC. From our model, the estimated total across 64°N below $\sigma_\Theta = 27.8$ is with 0.8 Sv too low [about 3 Sv; cf. with Hansen and Østerhus (2000)].

Given that details of the overflow and exchange processes across the ridges are not simulated entirely realistically by the model, the question arises as to what extent optimal observations calculated with this configuration are of any practical value. To the first order the study serves as a demonstration of the approach. Since the main processes are present, the main patterns are expected to be present, but details may be different.

Figure 2 shows that the GSR ridge heat transport variability (northward heat transport is positive) is closely linked to the atmospheric variability as described by the North Atlantic Oscillation (NAO) index [i.e., the difference of normalized sea level pressures (SLP) between Ponta Delgada, Azores, and Stykkisholmur/Reykjavik, Iceland; see Hurell and van Loon (1997) for details]. A high NAO index is associated with stronger-than-average westerlies over the mid latitudes. It thus leads to an enhancement of the negative wind stress curl over the subpolar North Atlantic that in turn drives an anomalous barotropic circulation around Iceland (BKS), and thus determines the southward transport variability through DS.

Net southward volume transport through the DS is compensated by the northward volume flux of warm water over the ridges east of the strait. Anomalies of the southward volume transport through DS and the net heat transport over the GSR are thus strongly correlated. The maximum correlation between the NAO index and the GSR heat transport as displayed in Fig. 2 is 0.80 with 0 time lag, whereas the correlation with DS volume transport is lower (0.70) with a slight positive lag of about 5 months.

Figure 2 indicates that NAO variability has spectral power in the decadal band as well as in the interdecadal band on periods longer than 50 yr. The transport curves show less interdecadal variability but are noticeably affected by the decadal-scale atmospheric variations. In contrast, an interdecadal signal clearly dominates the time-series of temperatures that are being advected across the GSR. They are shown in Fig. 3 and represent basin-averaged temperature anomalies north and south of the sills. While a decadal signal is visible in the northern time series, the southern basin varies primarily on inter decadal periods. We note that both curves show distinct time lags with respect to the NAO index, with the temperature south and north of the sill leading and

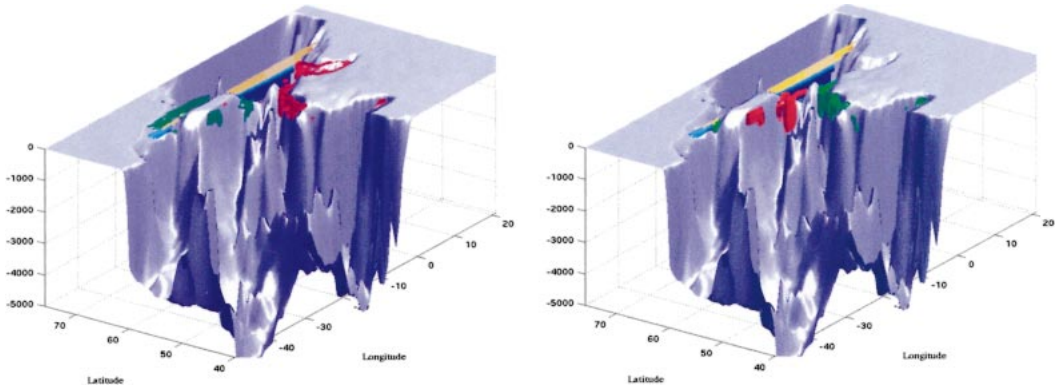

FIG. 4. Sensitivity of Feb meridional heat transport across the GSR with respect to the (left) 1 Jan temperature and (right) salinity initial conditions. The section, across which the heat transport is calculated, is marked in yellow and blue. Regions with small sensitivities are excluded from the graph. The red and green (positive and negative, respectively) isosurfaces are at 0.67 TW $°C^{-1}$ and 2.0 TW psu^{-1} for temperature and salinity, respectively.

lagging the NAO index by approximately 4 yr, respectively.

The basin-averaged temperature is affected by surface heat fluxes. The figure suggests, however, that the basin-averaged temperature anomalies to some extent are actually also an integrative consequence of anomalous cross-ridge heat transports, even on interdecadal time scales. Changes of the heat transport variability can be caused by volume transport anomalies or by changes in the advected temperature. It appears that on the decadal period heat transport changes are mainly due to volume transport anomalies, while the interdecadal variability is mostly due to changes in the advected temperature north and south of the sills. The latter are also affected by the transport anomalies. Persistently lower northward heat transports leads to decreasing temperatures north of the ridge, the temperature anomalies averaged over region north of the sills can (in our model, which has closed boundaries) in fact be explained solely by the diagnosed heat transport anomalies. Temperature anomalies south of the sill are probably more affected by overturning and heat transport anomalies farther south. Döscher et al. (1994) found a 3–4-yr time lag between temperature changes imposed south at the boundary just south of the sill and overturning anomalies at 48°N. A detailed interpretation of the processes involved in modifying the heat transport across the GSR is beyond the scope of the present work. However, their interpretation is important for an observing system design: anomalous cross-ridge heat transports create water mass anomalies that are subsequently carried around advectively in individual basins by the circulation. Observation points located remote from the ridge have thus the potential to record the history of the heat transport across the ridge, which enables the hindcast from observations taken afterward. The involved time scales probably enable reconstruction of at least a part of the signal from observation taken even a few years afterward. However, this will not be attempted in the following, which will consider only shorter time scales.

5. Optimal observations for the February GSR heat transport

What needs to be measured in the ocean to reconstruct the previously described heat transport variations across the GSR ridge that was described in the previous section? To answer this question we use the concept of optimal observations with the scalar h representing the February 1990 heat transport across the GSR. Optimal observations are equally suitable for forecast and hindcast situations, in fact their temporal distribution gives insight into which mode will perform best. From the discussion in the last section, it can be expected that future downstream observations may play a role for the determination of the heat transport.

In previous publications only adjoint sensitivities were used to obtain insight into an observing system design (e.g., Marotzke et al. 1999; Lee et al. 2002; Schröter and Wunsch 1986). Sensitivities of the February cross-ridge heat transport with respect to the 1 January temperature and salinity initial conditions are shown in Fig. 4. The figure shows a positive–negative sensitivity pattern for temperature and salinity between Iceland and Scotland which leads to consistent dynamic density anomalies. Both anomalies support an enhanced northward volume flux into the Norwegian Sea and thus an enhanced cross-ridge heat transport. In contrast, the pattern of negative sensitivity north of Iceland is only visible in temperature, which is passively advected through the DS.

Figure 5 shows optimal observations as the gradient of the GSR ridge heat transport with respect to monthly mean temperature observations for selected months of a 1-yr period. At the beginning of the assimilation period the distribution of optimal observations is similar to the

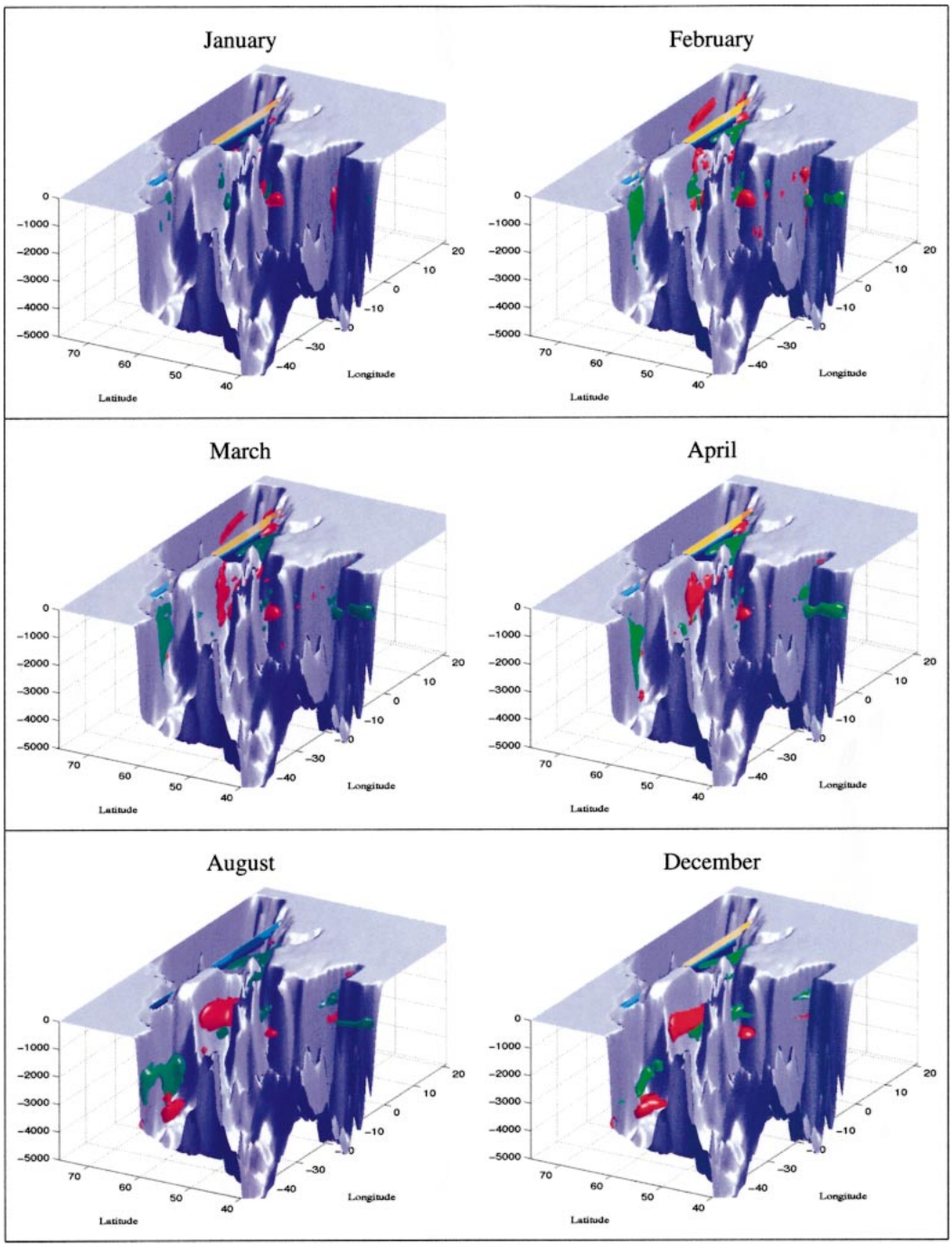

FIG. 5. Location of hydrographic observations that are optimal for inferring Feb meridional heat transport across the GSR. Red and green surfaces are isosurfaces (positive and negative, respectively) of the gradient of the heat transport with respect to temperature observations for the illustrated months. The gradient was multiplied with the square root of temperature error weight. The threshold for the isosurfaces is at ± 3.5 TW. Regions without optimal observations, i.e., without any noticeable impact on the cost function, are not shown in the figure. The section is marked in yellow and blue. The threshold value for the gradient $\partial h/\partial y$ was adjusted in order to have the same number of hydrographic data at optimal locations as the number of data sampled in a monthly section. The total number of data points in the 12 months is 7764 for temperature.

sensitivities shown in the previous figure. However, in February the signal of cold overflow emerges in the DS and begins to descend south of it in later months. The vertical mixing process and the descent to its final depth is also visible for the following month as a negative gradient gradually approaching deeper layers. In accord with the enhancement of a barotropic cyclonic gyre around Iceland that was discussed above, the cold DS signal is associated with an enhanced cross-ridge heat transport. The same is true for less southward IS overflow water which is documented by the positive gradient south of Iceland. The fact that the patterns are south and not north of the sill documents that there is no net northward flow through this strait. Negative gradients close to Scotland are due to a local wind-driven overturning cell east of Iceland. Because of the weighting with the temperature error profile, the distribution in Fig. 5 also gives information about size of the signal one could detect with these observations. The threshold value of 3.5 TW was selected to obtain the same number of optimal observation as on a monthly section for the performance comparison in section 6. Observations within the isosurfaces are thus likely to detect a signal smaller than 3.5 TW.

If one were to compute the December heat transport, sensitivities could then be calculated for all months of the year similar to Schröter and Wunsch (1986). However, they would still differ from optimal observations since the latter reflects only the influence of possible changes in the forcing fields and in the January initial conditions. Adjoint sensitivities describe the influence of many arbitrary changes of the hydrography that may not be represented by changes in forcing fields and January initial conditions.

Optimal observations are related to adjoint sensitivities as given by (13): the adjoint sensitivities are weighted by error matrices and propagated by the linearized forward model. Therefore, adjoint sensitivities describe only the causes of anomalies, whereas optimized observations blend causes and effects. For January, the month where the integration starts, both fields show similar patterns along the eastern boundary; however, optimal observations emphasize the deeper layers due to the additional weighting with the error matrices.

The distributions of optimal observations for the period after February are determined by the cross-ridge heat transport anomalies and subsequent advective processes. Optimal observation sites are very rare in January but accumulate toward the end of the year. This is because hydrographic measurements taken in December are influenced by the flow field throughout the entire year and thus provide maximum information about wind stress anomalies that, in turn, influence the cross-ridge heat and volume transports in February. January temperature anomalies influence the February cross-ridge heat transport kinematically and provide only little (or no) information about the wind stress forcing field. January density anomalies are of dynamical importance, for they enhance the inflow into the Norwegian Sea, but the effect of the enhanced exchange on the hydrography carries more important information about the cross-ridge transports. Because of the dominant control by wind stress conditions, the GSR heat transport has a large component that is not predictable from kinematics alone [in contrast to the suggestion of Marotzke et al. (1999) for the heat transport at 29°N].

6. Reconstruction of the GSR heat transport

In the previous section we discussed the distribution of optimal observations and their relation to physical mechanisms in the ocean. Here we will now provide a ''proof of concept'' by demonstrating in a twin experiment setup that optimal observations are indeed most efficient in reconstructing the GSR heat transport. To that end, hydrographic model fields taken from year 1990 serve as simulated data. The cost function is proportional to the quadratic model–data misfit of temperature and salinity at the respective positions where observations exist and will be minimized with the adjoint method. The assimilation period for all experiments is 1 yr. The control parameter set for the variational assimilation system comprises initial hydrographic conditions and monthly mean corrections for the surface flux fields. The first guess for the forcing and initial conditions were taken from model year 1965. The goal of the experiments is to reconstruct the heat transport across the GSR in 1990. The years 1965 and 1990 were selected since they represent extreme conditions of anomalous low and high GSR heat transport values (cf. Fig. 2).

We will discuss in this section the success of reconstructing the GSR heat transport based on three different data distributions: 1) temperature (T) and salinity (S) over the ridge only as would be the case for a hydrographic section; 2) optimal observations of T and S, which in most cases are located away from the location where the heat transport is being estimated; 3) T and S on the full model grid (only for the case of reconstructing February heat transport). To enable a quantitative comparison, the number of hydrographic data at optimal locations was chosen to be the same as the number of data in the monthly section; that is, the threshold for the gradient $\partial h/\partial y$ was adjusted to meet this condition.

In Fig. 6 we plot the difference between the true 1990 model heat transport and the reconstructed 1990 annual mean heat transport against the quadratic model–data misfit of the hydrographic observations. Results are provided for the two data distributions listed above: 1 and 2. Optimal locations were computed specifically for the annual mean GSR heat transport. The resulting distribution now includes the region south of the DS for most of the months with a yet smaller extent. This is in agreement with the view that the distribution is composed of an average of 12 distributions for each of the 12 months in the year, where each distribution is similar to the

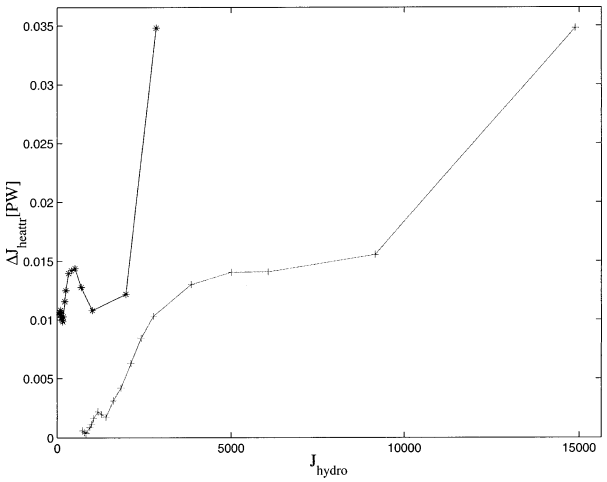

FIG. 6. Annual mean heat transport difference ΔJ_{heattr} in dependence of the cost function decrease J_{hydro}. ΔJ_{heattr} is calculated with respect to the annual mean value of the simulation of year 1990. First-guess initial condition and daily–twice daily forcing correspond to 1965. The use of monthly mean temperature and salinity along the section, across which the heat transport is defined, is denoted by ''*.'' The curve denoted by ''+'' corresponds to using same number of data points at optimal locations. The number of data points in the cost function is 15 526. Both optimizations were stopped after iteration 16.

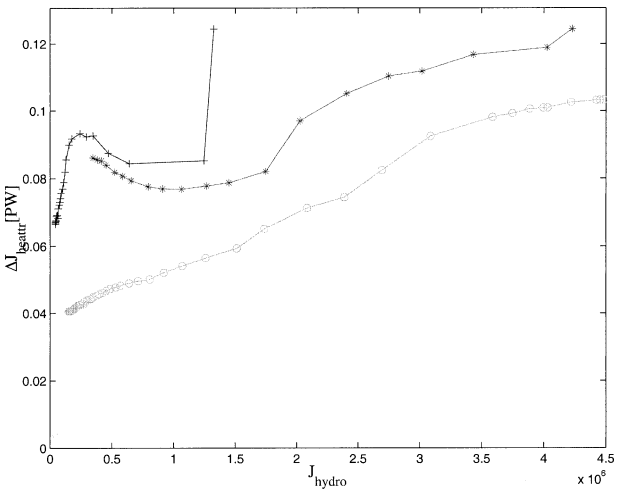

FIG. 7. Feb heat transport difference ΔJ_{heattr} (1990 − 1965) in dependence of the cost function decrease J_{hydro}; J_{hydro} composes optimal salinity and temperature data. The curves denoted with +, *, and ○ correspond respectively to experiments using optimal (same number as on the GSR section) and all available monthly mean data for the standard setup and an experiment without convective adjustment. The cost function values J_{hydro} were multiplied by a factor of 100 for display reasons.

distribution for the February heat transport shifted according to the specific month. Since each symbol represents individual iterations of the optimizations, the convergence rate of the optimization towards the true heat transport can be inferred from the curves as well. Both data distributions have skill in reconstructing 1990 annual mean heat transport. The significantly larger initial model–data misfit in case (2) indicates the associated larger sensitivity of the optimal observations to heat transport changes, which is expected, since simulated data and the first guess correspond by construction to low and high heat transport values, respectively. After normalizing the cost functions with the number of observations, its initial values of 1 and 0.2 are being reduced to values of about 0.05 and 0.005 after the optimization, respectively. The reconstruction of the annual-mean heat transport is almost perfect for the optimal data distribution after only about 10 iterations. Considering the prespecified error profiles for temperature and salinity, the minimum data accuracy required for the cost function to stay above the noise level is at 0.11°C and 0.022 psu for section data (iteration 10) and 0.33°C and 0.066 psu for optimal data (iteration 11). The estimates correspond to the surface error values, higher accuracy (smaller error values) are required for deeper layers. The values are well above CTD standards, but already quite challenging in terms of data assimilations where the error includes model and representation errors.

Analyzing the temporal evolution of the reconstructed 1990 heat transport (not shown) it becomes clear that the temporal heat transport fluctuations are not constrained at all by both previous data distributions, but still reflect the 1965 conditions. The largest discrepancy actually occurs during February, despite the fact that the annual mean heat transport was recovered successfully. To understand this puzzle, we investigate next whether a data distribution can be found that allows us to reconstruct the heat transport for an individual month—taken here to be February 1990—or if some systematic difficulty prevents the reconstruction of the circulation on shorter time scales.

Figure 7 shows the heat transport error as a function of the cost function value for the two different experiments corresponding to 1) an optimal data distribution (cf. Fig. 5) and 2) monthly mean temperature and salinity data available on the full model grid available for the 12-month period. Several findings are noteworthy from the figure. First, an optimal data distribution performs better than a complete temperature and salinity distribution. Moreover, in both cases the cross-ridge heat transport cannot be reconstructed successfully, in striking contrast to the previous annual-mean case. The heat transport error is reduced by more than 50% after assimilating optimal data. However, since the target value of year 1990 was anomalously high and the value corresponding to the first guess was anomalously low, the actual skill for the reconstructing of monthly mean heat transport is still quite low. The surprising degradation of the result upon the usage of basin-wide data coverage is likely due to the fact that most of the additional data do not contain any extra information about the heat transport. The lower overall sensitivity of the heat transport upon the convergence to the data leads to a slower

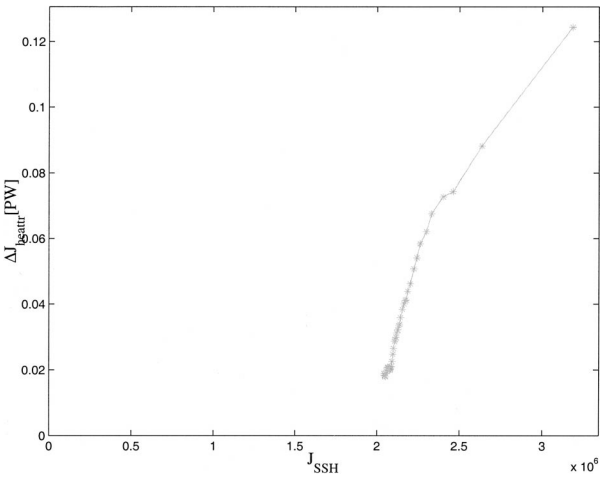

FIG. 8. Feb heat transport difference ΔJ_{heattr} (1990 − 1965) in dependence of the cost function decrease J_{SSH}; J_{SSH} includes daily SSH data.

heat transport convergence. Further improvement might be possible with additional iterations.

To understand the failure of reconstructing the heat transport, we performed an experiment that did not use convective adjustment. For this latter case, all comparison data and heat transport values are taken from a 1990 experiment without convective adjustment. Optimal locations were specifically calculated for a setup without adjustment. As Fig. 7 indicates, the remaining error of the heat transport is reduced to less than 40% and the simultaneous reduction of the cost function suggests a now closer link between hydrographic data and cross-ridge transports than was previously obvious with an active convective adjustment scheme.

Convective adjustment plays an important role in the forward model where it transports the overflow signal toward depth. The corresponding convection process of the adjoint model transports the model data misfit information of the overflow signal back to shallow depth and enables the estimation of surface wind stress corrections. However, this is only true if overflow and convection takes place in the forward run around which the adjoint is linearized. The first-guess simulation uses 1965 forcing, which leads to low February heat transport and is characterized by almost no overflow and thus no convection in February. Because of the lack of the process that transports the information to the surface, the signal about the February 1990 overflow remains hidden at depth. This is a general problem of the linearization approach of the adjoint method. Nevertheless, optimal observations shown in Fig. 5 still give the correct locations since the construction uses a finite difference approximation instead of the linearized forward model. This problem has less influence on the estimation on longer time scales (as with the annual mean). High heat transport variability ensures the existence of convection events. Convectively driven mixing may render hydrographic observations less effective if convective adjustment processes are not the same in the simulation and in the real ocean. This is the case for the estimation of the cross-ridge heat transport and might also be true for state estimations in general.

7. SSH versus hydrographic data

The close relation between GSR heat transport variability and the wind stress curl variability (BKS) around Iceland suggests that the success of transport estimations mainly depend on the ability to estimate this wind stress. In this section we will expand the previous discussion by comparing the impact of hydrographic data with that of sea surface height data on reconstructing the cross-ridge heat transports and wind forcing.

As indicated from the distribution of optimal observations in Fig. 4, February GSR heat transport anomalies leave a distinct downstream trace in the temperature field. In principle, the adjoint method transforms this information into wind stress improvements. However, results from the previous section demonstrate that the monthly transport cannot be fully recovered when missing convective adjustment prevents the transfer of information from the deep ocean to the surface. In contrast, sea surface height (SSH) observations represent a surface signature of the underlying circulation and do not suffer from this restriction.

In the following we use daily SSH data to reconstruct the February 1990 heat transport. The result of the optimization is shown in Fig. 8, again as heat transport differences versus cost function values. The figure shows that the heat transport can be reconstructed almost perfectly with a relation between heat transport error and cost function misfit that is almost linear. Note that only a small reduction of the SSH misfit is associated with an almost correct estimation of the heat transport. Only monthly mean corrections of the surface fluxes are estimated so that only the monthly mean part of the SSH variability can be expected to be matched.

SSH observations that are optimal for reconstructing the February cross-ridge heat transport are shown in Fig. 9. The overflow temperature signal visible in Fig. 5 emerging from the DS and the IFR is now clearly visible as a sea level depression pulse that travels around the Cape Farewell and the Rikjanes Ridge (cf. also discussion in BKS). Equally important is the positive signal along the eastern boundary, especially in the first month, where it reflects the density anomalies brought in by changes of the initial condition as shown in Fig. 4. The positive anomaly subsequently propagates northward and reaches across the GIN sea as a consequence of the anticyclonic barotropic circulation in that part of the basin. Obviously physical processes which are represented by hydrographic data have a corresponding sig-

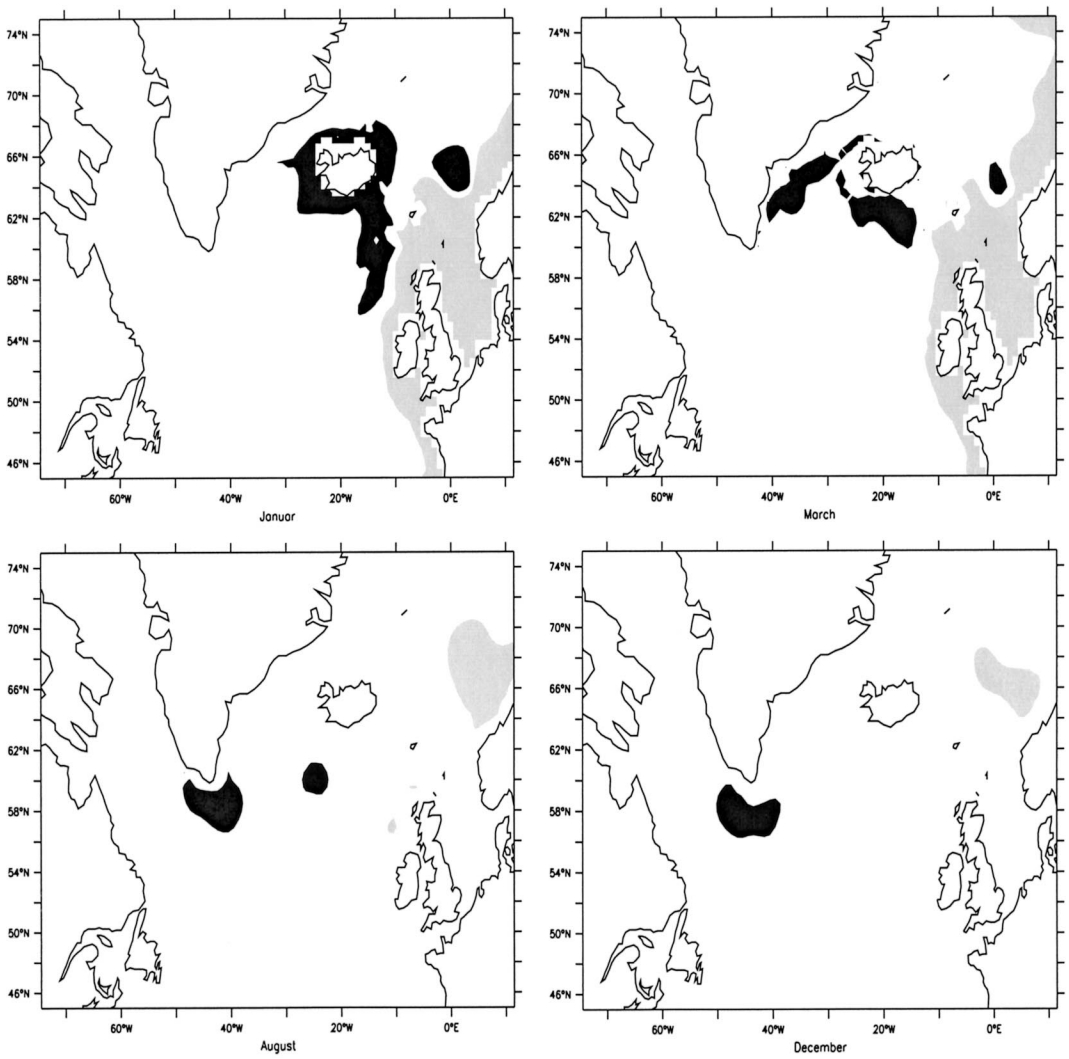

FIG. 9. Gradient of the Feb meridional heat transport with respect to SSH observations. Black and gray patterns correspond to negative and positive response of the sea surface, respectively. The contours are at ± 2.1 TW cm^{-1} for a spatially uniform SSH error of 5 cm.

nature in the SSH data. However, SSH fields have a closer link to wind stress data than hydrographic observations and constrain the estimation of the wind stress with the adjoint method much more efficiently. By multiplying the gradient in Fig. 5 with the SSH error, one obtains a value for heat transport variations that are detectable with the data. That means for Fig. 5 that variations smaller than 10 TW are detectable with data inside the patterns.

In our model world, ''observations'' of true daily or monthly means are feasible, whereas real measurements are often made at a specific date and may not be representative for more than a few days. In our model configuration the heat transport varies on a daily time scale but SSH periods in the region of the East Greenland current are typically 1–2 weeks. SSH observations integrate and thus filter the heat transport variability. Observing SSH fields at a rate of about every few days would be sufficient to determine the transport variability. This is close to what the current multisatellite configuration provides. For hydrographic measurements, chances for a sufficient coverage are lower. The traveling SSH anomaly in Fig. 9 corresponds to a heat transport anomaly of a specific month and the spatial distribution of multiple SSH pulses taken from a single snapshot may record a whole time series of heat transport variations. Given that the successful reconstruction of the transport is based on perfect data and a perfect model (identical twin framework), perspectives are lower for the performance in reality. On the other hand, we only used data that contribute mostly to the reconstruction of the heat transport. In practice, more data sources and better forcing (especially inadequate forcing and initial conditions were chosen in our experiments) are available and even plain simulations would have some skill, wherefore the appropriate question is not whether

a reconstruction is possible from the chosen data but whether an already skillful estimation can be improved.

8. Conclusions

The design of a climate observing system is an important element of ocean state estimation. In contrast to existing design approaches that use adjoint sensitivities, the design problem was discussed here in the context of optimal observations that emerge as singular vectors from the data resolution matrix. It was shown that in the limit of large observational errors, an approximation of optimal observations for scalar quantities can be calculated essentially by one run of the adjoint and one additional forward run of the linearized forward model. Although the limits of large observational errors rarely apply, the observations calculated for this limit were shown to apply equally well beyond the limit.

An important result, obtained here for the example of reconstructing the heat transport across the GSR, is that optimal observations are most efficient in constraining the optimization problem and in particular perform significantly better than can be achieved by using section data or even basin-wide data. This is counterintuitive but can be understood in that those additional data, while not carrying more information about the GSR heat transport, do complicate the shape of the cost function and thus degrade the performance of the procedure. For understanding the sampling problem of the ocean this is an important result: well-selected observations seem significantly more valuable than random coverage or even full coverage. However, while interpreting this result we have to recall that the distribution depends not only on the quantity of interest (GSR heat transport in our example) but also on the model and the assimilation framework (e.g., the choice of the weights, the controls and the length of the assimilation interval).

Another important result is that in our context of the GSR heat transport estimates, SSH data provide more robust information than hydrographic data, at least on shorter time scales. The reason is that different dynamical regimes may be represented in the data than in the model first guess, which in turn may reduce the value of hydrographic data for the estimation of surface flux fields required to reconstruct the GSR heat transport. This was shown to hold for convective adjustment, but can be expected to be the case also for many other processes. Therefore optimal observations have to be used with care since they describe only local properties and do not guaranty skill for the estimation of the quantity they are designed for, even though they may represent the associated physical processes well.

We note that optimal observations describe causes and effects of anomalies of a scalar quantity. In case of the GSR heat transport, the pathways of the overflow water through the DS and FSC is clearly emphasized in the position of optimal observations. Those hydrographic conditions are also reflected in the sea level fields as negative gradient signal which is related to a SSH depression pulse that travels around Cape Farewell. Their value is apart from identifying key regions in providing a new tool for studying the causes and effects of anomalies of integral quantities.

The distribution of optimal observations is generally quite complex and problematic to sample by standard in situ observational tools. Optimal observations are probably of limited help, in terms of seeding strategies for floats and drifters, because the floats are expected to leave the key regions rapidly. Embedding float trajectories into the assimilation, which is not yet addressed could lead to optimal float seeding distributions which is likely to also result in a very stringent seeding strategy. However, not all details of the structures may necessarily be resolved in a survey and spatial coherence of optimal observations enable a less dense sampling than indicated by the distribution. The value will be more in providing guidelines than an exact distribution. For the GSR heat transport, we could learn that transport variations are better recorded downstream (e.g., by moorings at the center of the optimal observation sites) than on a section.

Moreover, since optimal observations are defined as the gradient of a specific scalar quantity with respect to a data distribution, they enable us to make a priory decisions as to whether a specific signal can be detected from data. Yet, the method for calculating optimal observation is limited by the validity of the linearization and cannot be applied with models obeying chaotic dynamics for periods longer than the predictability of the model. However, the same limitation applies to the usefulness of adjoint models for finding the minimum of the cost function in the adjoint method (Li 1991; Stensrud and Bao 1992). The applicability of our method for observing system design is therefore well imbedded in the limitations of the state estimation procedure where time scales of many years are feasible (Stammer et al. 2002).

Little may have been learned here regarding optimal observations for the GSR heat transport since mainly expected features of the circulation were revealed and because we limited our experiments to only one year. However, we consider the value of the present work to be in providing confidence that the structures are quasi-optimal, as well as confidence in the physical signal they carry associated with anomalies of certain scalar quantities.

Acknowledgments. We thank Bruce Cornuelle for valuable comments and an anonymous reviewer for inspiring remarks. Computational support from the National Partnership for Computational Infrastructure (NPACI) and the National Center for Atmospheric Research (NCAR) is acknowledged. This work was supported through ONR (NOPP) ECCO Grants N00014-99-1-1049 and through NASA Grant NAG5-8623. This is a contribution of the Consortium for Estimating the

Circulation and Climate of the Ocean (ECCO) funded by the National Oceanographic Partnership Program.

REFERENCES

Adcroft, A., C. Hill, and J. Marshall, 1997: Representation of topography by shaved cells in a height coordinate ocean model. *Mon. Wea. Rev.,* **125,** 2293–2315.

Bacon, S., 1998: Decadal variability in the outflow from the Nordic seas to the deep Atlantic Ocean. *Nature,* **394,** 871–874.

Baker, N. L., and R. Daley, 2000: Observation and background adjoint sensitivity in the adaptive observation-targeting problem. *Quart. J. Roy. Meteor. Soc.,* **126,** 1431–1454.

Barth, N., and C. Wunsch, 1990: Oceanographic experiment design by simulated annealing. *J. Phys. Oceanogr.,* **20,** 1249–1263.

Bennett, A. F., 2002: *Inverse Modeling of the Ocean and Atmosphere.* Cambridge University Press, 352 pp.

Berliner, L. M., Z.-Q. Lu, and C. Snyder, 1999: Statistical design for adaptive weather observations. *J. Atmos. Sci.,* **56,** 2536–2552.

Biastoch, A., R. Käse, and D. Stammer, 2003: The sensitivity of the Greenland–Scotland Ridge overflow to forcing changes. *J. Phys. Oceanogr.,* **33,** 2307–2319.

Dickson, B., I. Yashayaev, J. Meincke, and B. Turrell, 2002: Rapid freshening of the deep North Atlantic Ocean over the past four decades. *Nature,* **416,** 832–836.

Dickson, R. R., and J. Brown, 1994: The production of North Atlantic Deep Water: Sources, rates and pathways. *J. Geophys. Res.,* **99,** 12 319–12 341.

Döscher, R. C., C. W. Böning, and P. Herrman, 1994: Response of circulation and heat transport in the North Atlantic to changes in forcing in northern latitudes: A model study. *J. Phys. Oceanogr.,* **24,** 2306–2320.

ETOPO5, 1988: Digital relief of the surface of the earth. Data Announcement 88-MGG-02, NOAA National Geophysical Data Center.

Fu, L.-L., and A. Cazenave, 2001: *Satellite Altimetry and Earth Sciences: A Handbook of Techniques and Applications.* Academic Press, 463 pp.

Fukumori, I., 2001: Data assimilation by models. *Satellite Altimetry and Earth Sciences,* L.-L. Fu and A. Cazenavo, Eds., Academic, 237–266.

Giering, R., and T. Kaminski, 1998: Recipes for adjoint code construction. *ACM Trans. Math. Software,* **24,** 437–474.

Gilbert, J. C., and C. Lemaréchal, 1989: Some numerical experiments with variable-storage quasi-Newton algorithms. *Math. Programm.,* **45,** 407–435.

Hansen, B., and S. Østerhus, 2000: North Atlantic–Nordic Seas exchanges. *Progess in Oceanography*, Vol. 45, Pergamon, 109–208.

——, W. R. Turrell, and S. Østerhus, 2001: Decreasing overflows from the Nordic seas into the North Atlantic Ocean through the Faroe Bank channel scince 1950. *Nature,* **411,** 927–930.

Hurell, J. W., and H. van Loon, 1997: Decadal variations in climate associated with the North Atlantic Oscillation. *Climate Change,* **36,** 301–326.

Jerlov, N. G., 1968: *Optical Oceanography.* Elsevier, 199 pp.

Kalnay, E., and Coauthors, 1996: The NCEP/NCAR 40-Year Reanalysis Project. *Bull. Amer. Meteor. Soc.,* **77,** 437–471.

Käse, R., and A. Oschlies, 2000: Flow through Denmark Strait. *J. Geophys. Res.,* **105,** 28 527–28 546.

Kleeman, R., and A. M. Moore, 1997: A theory for the limitation of ENSO predictability due to stochastic atmospheric transients. *J. Atmos. Sci.,* **54,** 753–767.

Lee, T., I. Fukumori, D. Menemenlis, Z. Xing, and L.-L. Fu, 2002: Effects of the Indonesian Throughflow on the Pacific and Indian Oceans. *J. Phys. Oceanogr.,* **32,** 1404–1429.

Levitus, S., and T. P. Boyer, 1994: *Temperatures.* Vol. 4, *World Ocean Atlas 1994,* NOAA Atlas NESDIS 4, 117 pp.

——, R. Burgett, and T. P. Boyer, 1994: *Salinity.* Vol. 3, *World Ocean Atlas 1994,* NOAA Atlas NESDIS 3, 99 pp.

Li, Y., 1991: A note on the uniqueness problem of variational adjustment approach to four-dimensional data assimilation. *J. Meteor. Soc. Japan,* **69,** 581–585.

Marotzke, J., R. Giering, Q. K. Zhang, D. Stammer, C. N. Hill, and T. Lee, 1999: Construction of the adjoint MIT ocean general circulation model and application to Atlantic heat transport sensitivity. *J. Geophys. Res.,* **104,** 29 529–29 548.

Marshall, J., A. Adcroft, C. Hill, L. Perelman, and C. Heisey, 1997: A finite-volume, incompressible Navier Stokes model for studies of the ocean on parallel computers. *J. Geophys. Res.,* **102,** 5753–5766.

Menke, W., 1989: *Geophysical Data Analysis: Discrete Inverse Theory.* Academic Press, 289 pp.

Palmer, T. N., 1998: Nonlinear dynamics and climate change: Rossby's legacy. *Bull. Amer. Meteor. Soc.,* **79,** 1411–1423.

Paulson, C. A., and J. J. Simpson, 1977: Irradiance measurements in the upper ocean. *J. Phys. Oceanogr.,* **7,** 952–956.

Roemmich, D., and W. B. Owens, 2000: The Argo Project: Global ocean observations for understanding and prediction of climate variability. *Oceanography,* **13,** 45–50.

Schröter, J., and C. Wunsch, 1986: Solution of nonlinear finite difference ocean models by optimization methods with sensitivity and observational strategy analysis. *J. Phys. Oceanogr.,* **16,** 1855–1874.

Snyder, C., 1996: Summary of an informal workshop on adaptive observations and FASTEX. *Bull. Amer. Meteor. Soc.,* **77,** 953–961.

Stammer, D., and C. Wunsch, 1996: The determination of the large-scale circulation of the Pacific Ocean from satellite altimetry using Green's functions. *J. Geophys. Res.,* **101,** 18 409–18 432.

——, and Coauthors, 2002: Global ocean circulation during 1992–1997, estimated from ocean observations and a general circulation model. *J. Geophys. Res.,* **107,** 3118, doi: 10.1029/2001JC000888.

——, and Coauthors, 2003: Volume, heat and freshwater transports of the global ocean circulation 1992–1997, estimated from a general circulation model constrained by WOCE data. *J. Geophys. Res.,* **108,** doi:10.1029/2001JC001115.

Stensrud, D. J., and J. W. Bao, 1992: Behaviors of variational and nudging techniques with a chaotic low-order model. *Mon. Wea. Rev.,* **120,** 3016–3028.

Wunsch, C., 1996: *The Ocean Circulation Inverse Problem.* Cambridge University Press, 442 pp.